Enhanced conversion reaction of Na-Cu-PO$_3$ via amorpholization and carbon-coating for large Na storage

Yongseok Lee [a, b], Jungmin Kang [a, b], Jinho Ahn [a, b], Wonseok Ko [a, b], Hyunyoung Park [a, b], Jung-Keun Yoo [c], Won-Sub Yoon [a, b, *], Jongsoon Kim [a, b, **]

[a] Department of Energy Science, Sungkyunkwan University, Suwon, 16419, Republic of Korea
[b] SKKU Institute of Energy Science and Technology (SIEST), Sungkyunkwan University, Suwon, 16419, Republic of Korea
[c] Carbon Composites Department, Composites Research Division, Korea Institute of Materials Science (KIMS), 797 Changwondaero, Changwon, Republic of Korea

ARTICLE INFO

ABSTRACT

Conversion-type cathodes have a higher theoretical capacity compared to intercalation-type cathodes due to the use of more transition metal cations. However, their sluggish kinetics and low operation voltage hinder their practical application in the industry, resulting in low specific capacity. To address these issues, we prepare an amorphous carbon-coated Cu(PO$_3$)$_2$ nanocomposite, and evaluate its electrochemical performance under rechargeable Na-ion battery system. At a current density of 24 mA/g, it achieves a large specific capacity of ~232 mAh/g with an average operation voltage of ~2.0 V (vs. Na$^+$/Na). Furthermore, the amorphous carbon-coated Cu(PO$_3$)$_2$ nanocomposite exhibits a cycle retention of ~90% compared to the initial capacity after 100 cycles. In contrast, bare Cu(PO$_3$)$_2$ shows poor electrochemical performance under the same conditions. Various experimental measurements have demonstrated that the amorphous carbon-coated Cu(PO$_3$)$_2$ nanocomposite exhibits a reversible and smooth conversion reaction of Cu(PO$_3$)$_2$ phase in the rechargeable Na-ion battery system.

© 2023 Elsevier Ltd. All rights reserved.

1. Introduction

By environmental pollution by usage of fossil fuels, it is important to develop the eco-friendly energy resources and efficient energy storage systems (ESSs) in the world [1,2]. Li-ion batteries have been widely used and their application gets larger from the small electronic devices to large-scale application such as electric vehicles (EVs) [3,4]. By limited Li resources, however, it is difficult to satisfy the LIB demands growing explosively, which leads to high production cost of LIBs. Thus, many researchers have studied development of low-cost and efficient rechargeable batteries for grid-scale energy storage [5,6]. Recently, rechargeable sodium-ion batteries (RSBs) have great attention, due to their low production cost by unlimited Na resources and monovalent-ion-based reaction mechanism like LIBs [7,8]. In terms of cathode materials for RSBs, the intercalated-based compounds, such as layered-type transition

metal (TM) oxides [9], polyanion [10], etc. have been widely studied, owing to their high redox potential. However, intercalation-based cathode materials for RSBs can just store 1 mol Na$^+$ per 1 mol TM ions [11,12]. For longer usage of rechargeable batteries after one charging process, it should be required to increase the available amounts of Na$^+$ per 1 mol TM ions in the cathode materials during charge/discharge [13].

To increase the Na$^+$ storage amounts per 1 mol TM ions in the material, the conversion-type compounds can be regard as one of the best choices. Unlike intercalation-type compounds that only use less than 1 mol Na$^+$ per 1 mol TM ions, conversion-type compounds can store at least 2 mol Na$^+$ per 1 mol TM ions during charge/discharge, which enables larger available capacities of conversion-type compounds than those of intercalation-type compounds [14,15]. However, several significant issues should be solved for conversion-type compounds to be applied as the cathode for RSBs. The first issue is their low operation voltage of below 1 V, which is the reason why the conversion-type compounds have been mainly used for anodes rather than cathodes [16,17]. The second issue is their poor ionic/electronic conductivities related to long ion diffusion length hindering the smooth kinetics in

electrochemical reactions [18,19]. The third issue is the large volume change and structural degradation during charge/discharge, which leads to the poor cycle performance [20,21]. Without overcoming these problems of the conversion-type materials, their practical utilization as the cathode in RSBs is difficult to achieve.

Our strategy to increase the operation voltage of conversion-type compounds is application of polyanion-based compounds. It was known Fe^{2+}/Fe^{3+} redox reaction in olivine $LiFePO_4$ can be occurred at higher operation voltage of ~3.4 V (*vs.* Li^+/Li) than that in the layered-type TM oxide, owing to the inductive effect by phosphorus ions with high electronegativity [22,23]. Thus, we thought polyanion compounds containing phosphorus with oxygen in the structure can also deliver the high redox potential during the conversion reaction. Moreover, it was reported Cu has lower negative standard enthalpies of formation compared to other transition metals, indicating that Cu-based compounds can exhibit higher redox potential than other TM-based compounds [14]. Furthermore, optimizing the particle architecture is an effective way to reduce the barrier to achieving the best performance. Amorphous materials with randomly linked clusters have been reported as promising electrodes, highlighting their intrinsic merits [24]. Compared to crystallite materials, amorphous materials have attractive advantages when used as cathodes for RSBs, including (1) facilitating Na^+ diffusion [25,26], (2) increasing Na^+ storage sites and diffusion channels [27,28], and (3) improving reaction activity [29,30]. Additionally, when conductive carbon is added during the high energy ball-milling process to obtain an amorphous phase, it forms a homogeneous carbon coating on the particle surface, which can be expected to improve electrical conductivity and suppress volume expansion [31,32].

For these reasons, we prepared an amorphous $Cu(PO_3)_2$ with conductive carbon nanocomposite (*a-c*-CPO), and it exhibited outstanding electrochemical performances as the novel conversion-type cathode for RSBs. Through combined studies using first-principles calculation and various experiments, it was revealed *a-c*-CPO exhibited the average operation voltage of ~2 V (*vs.* Na^+/Na) through the following conversion reaction of $Cu(PO3)_2$ phase in the nanocomposite under the RSB system; $Cu(PO_3)_2 + 2Na^+ + e^- \leftrightarrow Cu + 2NaPO_3$. At a current density of 24 mA/g, the *a-c*-CPO electrode delivered the large available capacity of ~232 mAh/g corresponding to 2 mol Na^+ storage. Even at 960 mA/g, its capacity was maintained up to ~61% of the capacity measured at 24 mA/g. Moreover, *a-c*-CPO showed the capacity retention of ~90% compared to the initial capacity after 100 cycles. These results indicates outstanding power-capability and cyclability of *a-c*-CPO as the novel conversion-type cathode for RSBs. In addition, the conversion reaction mechanism of $Cu(PO_3)_2$ phase under the RSB system was clearly demonstrated through the various *ex-situ* analyses using X-ray diffraction (XRD), high-resolution transmission electron microscopy (HRTEM), X-ray photon spectroscopy (XPS) and synchrotron-based X-ray absorption spectroscopy (XAS).

2. Experimental

2.1. Preparation of a-c-CPO

The bare $Cu(PO_3)_2$ was prepared by mixing raw materials such as CuO (Sigma Aldrich, 99%) and $(NH_4)_2HPO_4$ (Sigma Aldrich, 98%) in a molar ratio of 1:2. A total weight of 10 g of precursors, 100 ml of acetone and 12 Zr balls were collected in Nalgene bottle and uniformly mixed by wet ball-milling at 250 rpm for 12 h. After mixing, the resulting mixture was stirred on a hot plate at 60 °C for 12 h. Then, pellets from dried powder were heated at 850 °C for 12 h in air to obtain bare $Cu(PO_3)_2$. To synthesize the *a-c*-CPO composite,

the bare $Cu(PO_3)_2$ and conductive carbon were placed in a silicon nitride planetary bowl with 30 nitride balls of a diameter of 10 π and ball-milled at 500 rpm for 12 h. After the first ball-milling, a second ball-milling was performed at 500 rpm for 12 h using the collected composite material and 10 nitride balls of a diameter of 3 π. The completed *a-c*-CPO composite was composed of 80 wt% of $Cu(PO_3)_2$, 19 wt% of Super P carbon black, and 1 wt% of carbon nanotubes (CNTs).

2.2. Materials characterization

The bare $Cu(PO_3)_2$ and *a-c*-CPO composites were characterized using XRD (PANalytical) with Cu Kα radiation (wavelength = 1.54178 Å). The 2θ range was $10°-60°$ with a time per step of 0.13. The morphology of the materials and EDS elemental mapping were examined using SEM (SU-8010). HR-TEM particle images and SAED patterns measured using high-resolution transmission electron microscopy (HR-TEM; JEM-3010) at the National Center for Inter-university Research Facilities (NCIRF) at Seoul National University. The $Cu(PO_3)_2$ powder was analyzed using the inductively coupled plasma (ICP)-atomic emission spectrometer. The ac perturbation signal was ±5 mV and the frequency range were from 10-2 Hz-106 Hz. X-ray photon spectroscopy (XPS) characterization was performed using a K-alpha (Thermo Scientific Inc., U.K) model with Al Kα radiation (hv = 1486.6 eV). All the XPS spectra were referenced to the C1s at the binding energy (BE) of 284.8 eV. The overall conversion reaction was revealed using XANES and EXASF spectroscopy that performed at beamline 8C at the 3.0-GeV Pohang Light Source. The impedance of each sample was analyzed from 5 MHz to 500 mHz using a multichannel impedance analyzer system (VSP-300, Bio-Logic, Grenoble, France).

2.3. Electrochemical characterization

The *a-c*-CPO electrodes were fabricated from a slurry of 87.5 wt% *a-c*-CPO composite, 2.5 wt% Super-P carbon, and 10 wt% polyvinylidene fluoride (PVDF) binder in *N*-methyl-2-pyrrolidone (NMP), with a final ratio of 70 : 20: 10 = $Cu(PO_3)_2$: conductive carbon: PVDF binder, respectively. To ensure a fair comparison of the electrochemical performance between the *a-c*-CPO and bare $Cu(PO_3)_2$ electrodes, the same mass ratio of 70 wt% $Cu(PO_3)_2$, 20 wt% conductive carbon, and 10 wt% PVDF binder was used on bare $Cu(PO_3)_2$ electrode. The slurry was applied on Al foil with an areal mass loading of ~2 mg cm^{-2} and dried in an oven at 110 °C for 12 h. R2032 cells were assembled in an Ar-filled glove box using the *a-c*-CPO or bare $Cu(PO_3)_2$ composite electrode, a Na counter electrode, a separator (Whatman GF/F glass fiber), and an electrolyte (1.0 M $NaPF_6$ in diethylene glycol dimethyl ether (DEGDME)). The electrochemical performance of each cell was evaluated by charging and discharging in the voltage range of $1.0-4.0$ V at 30 °C using an automatic battery charge/discharge test system (WBCS 3000, WonATech). In full-cell testing, the anode used was the sodiated hard carbon electrode instead of Na metal. The electrode was prepared using the same procedure and ratio as the *a-c*-CPO electrode, except the usage of Cu foil. To minimize the irreversibility at the initial cycle, the hard carbon anode electrode was discharged to 0.001 V (*vs.* Na^+/Na) during the preparation of the sodiated hard carbon. Subsequently, the full-cell was fabricated using the *a-c*-CPO electrode as the cathode and the sodiated hard carbon as the anode. To minimize the irreversibility of the hard carbon, the electrode was pre-cycled by direct contact with Na metal in 1.0 M $NaPF_6$ in diethylene glycol dimethyl ether (DEGDME) electrolyte. Finally, R2032 coin-type full-cells were assembled in an Ar-filled glove box using the *a-c*-CPO cathode and pre-cycled hard carbon anode, with a capacity ratio of negative and positive electrodes of ~1.2.

2.4. Computational details

DFT calculations [33] were performed using the Vienna *Ab Initio* Simulation Package (VASP). We used projector-augmented wave (PAW) pseudopotentials were used [34] with a plane-wave basis set, as implemented in VASP. Perdew−Burke−Ernzerhof (PBE) parametrization of the generalized gradient approximation (GGA) [35,36] was used for the exchange-correlation functional. All the calculations were performed with an energy cutoff of 520 eV until the remaining force in the system converged to less than 0.02 eV Å^{-1} per unit cell. The parameters reported in the Materials Project database [37] such as the U values and energy cutoff values, were used for the DFT calculation.

3. Results and discussion

Fig. 1 presents a schematic image of the preparation process for *a-c*-CPO from bare $Cu(PO_3)_2$, along with the merits of amorphous materials. To achieve amorpholization and carbon coating simultaneously, bare $Cu(PO_3)_2$ was pulverized and mixed with conductive carbon through high energy ball-milling. Unlike crystalline materials with an ordered structure, the amorphous phase with mainly a disordered structure has inherent advantages, including the fast Na^+ diffusion with more diffusion channels and the improved reaction activity. Additionally, the nano-scaling process, which naturally accompanies the process of achieving amorpholization, provides shorter diffusion pathways for smooth Na^+ diffusion and an enlarged surface area where the electrolyte and active material can contact each other. Consequently, it is expected that these characteristics of an amorphous structure can deliver improved electrochemical performances compared to the

crystalline structure. Furthermore, the carbon layers on particle surfaces enhance electrical conductivity, improve the surface chemistry of active material, and act as a barrier to direct contact with the electrolyte. The carbon contents were confirmed through thermogravimetric analysis (TGA) as ~20 wt% in *a-c*-CPO, indicating that *a-c*-CPO is composed of ~80 wt% of $Cu(PO_3)_2$ and ~20 wt% of conductive carbons (Fig. S1). It is expected that *a-c*-CPO, which is completely prepared with these changes, can exhibit outstanding electrochemical performance, overcoming the drawbacks of the conversion-type compounds under the RSB system.

The material identification and morphological analyses of *a-c*-CPO were performed using X-ray diffraction (XRD) patterns of bare $Cu(PO_3)_2$ (shown in Fig. 2a), which exhibited a clear crystalline structure with sharp and high intensity of XRD peaks indicating the $C\,2/c$ space group. Owing to the high energy ball milling process, *a-c*-CPO showed the broad and unobvious diffraction peaks, indicating the formation of an amorphous phase across the overall regions. In addition, the intensity of XRD patterns, which reflects the crystallinity of the material, decreases as the level of disorder increases from bare $Cu(PO_3)_2$ to *a-c*-CPO. The total intensity of *a-c*-CPO was reduced by about 94% compared to that of bare $Cu(PO_3)_2$ at the same XRD measurement conditions, indicating a higher level of disordering in the *a-c*-CPO sample. Transmission electron microscopy (TEM) analyses (Fig. 2b−c) indicate selected area diffraction (SAED) patterns of bare $Cu(PO_3)_2$ phase showing clear reflection spots such as (022) or (42$\bar{2}$) planes representing a crystalline phase, which supports the XRD results. In contrast, there were no spots of a crystalline phase in the SAED pattern of *a-c*-CPO and just one ring-pattern related to (022) plane was detected, implying the completion of amorphous phase through high energy ball-milling. In contrast, there were no spots of a crystalline phase in the SAED
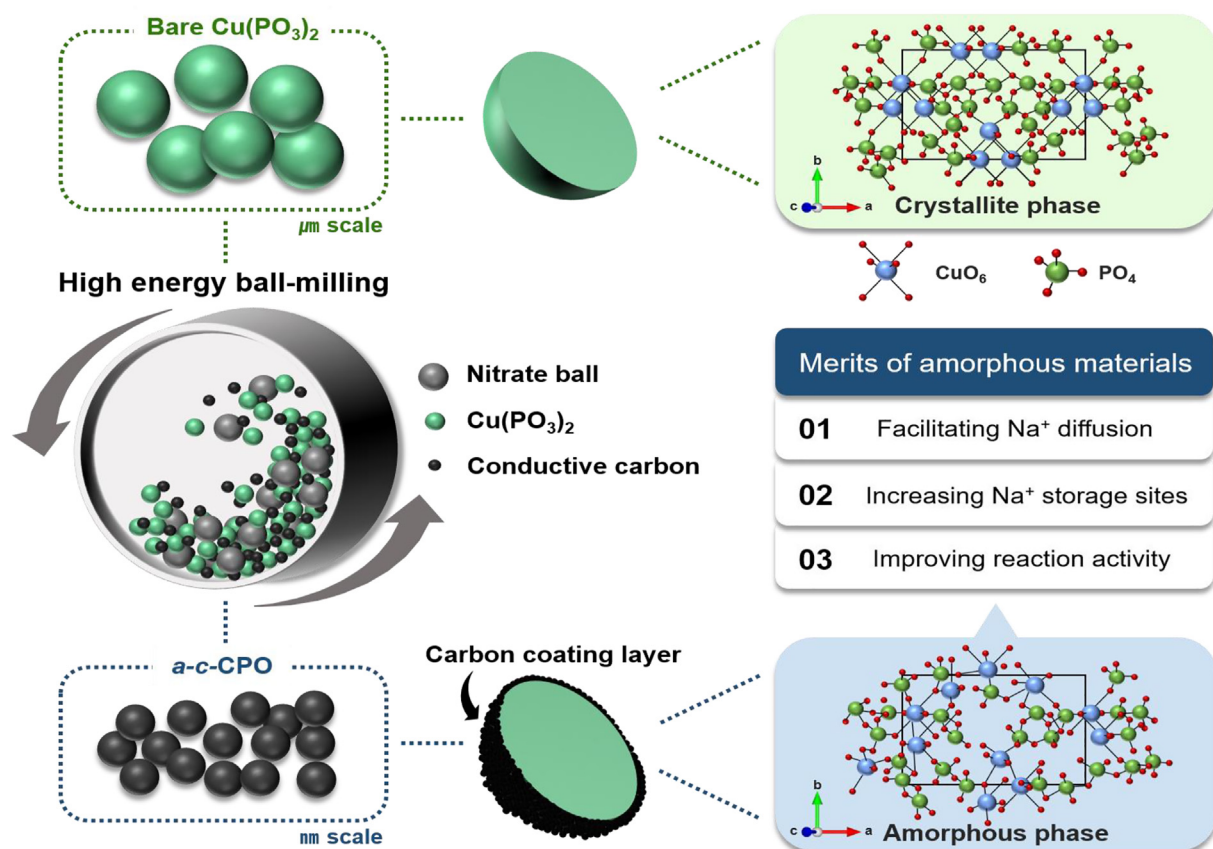

Fig. 1. Schematic image of the preparation process for *a-c*-CPO from bare $Cu(PO_3)_2$, along with the merits of amorphous materials.

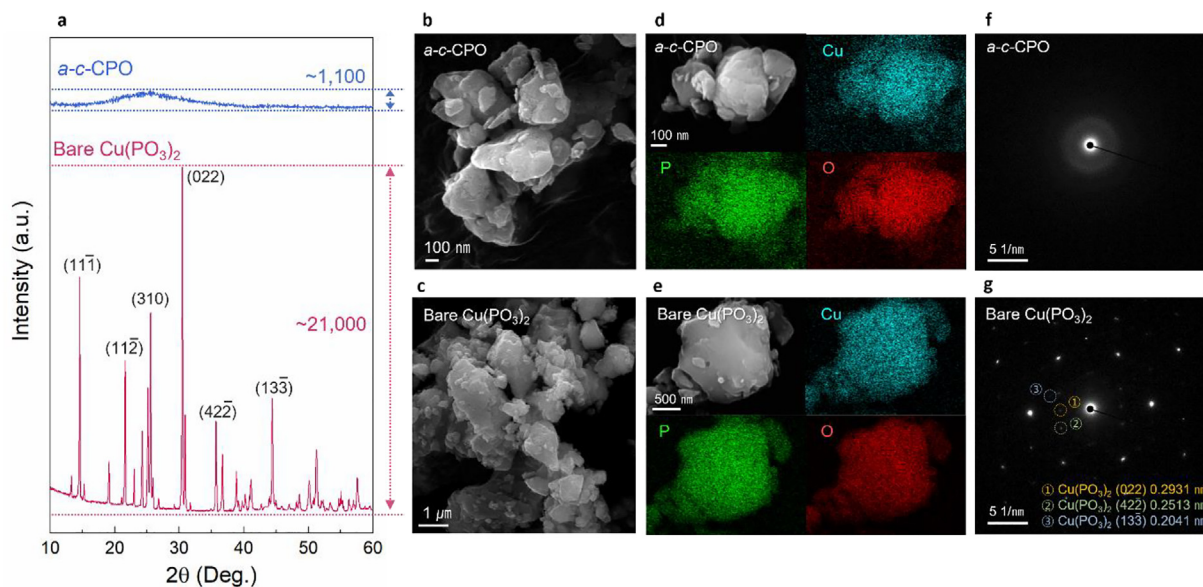**Fig. 2.** (a) The XRD patterns of *a-c*-CPO and bare $Cu(PO_3)_2$ with maximum intensities. SEM images of (b) *a-c*-CPO, (c) bare $Cu(PO_3)_2$. EDS elemental mappings (Cu: blue, P: green, O: red) of (d) *a-c*-CPO, (e) bare $Cu(PO_3)_2$. TEM-SAED patterns of (f) *a-c*-CPO, (g) bare $Cu(PO_3)_2$. (For interpretation of the references to color in this figure legend, the reader is referred to the Web version of this article.)

pattern of *a-c*-CPO and just one ring-pattern related to (022) plane was detected, implying the completion of amorphous phase through high energy ball-milling. At Fig. S2, XRD patterns of bare $Cu(PO_3)_2$ electrode showed clear diffraction peaks indicating its crystallinity despite a decrease in overall intensity after electrode fabrication with carbon mixing. In addition, the TEM image of the *a-c*-CPO electrode coated with carbon using high energy ball-milling displayed a carbon layer on the particle surface, whereas the bare $Cu(PO_3)_2$ electrode simply mixed with carbon during electrode fabrication showed distributed carbon around the particle, indicating the significance of the ball-milling process. The morphologies of bare $Cu(PO_3)_2$ and *a-c*-CPO were identified using scanning
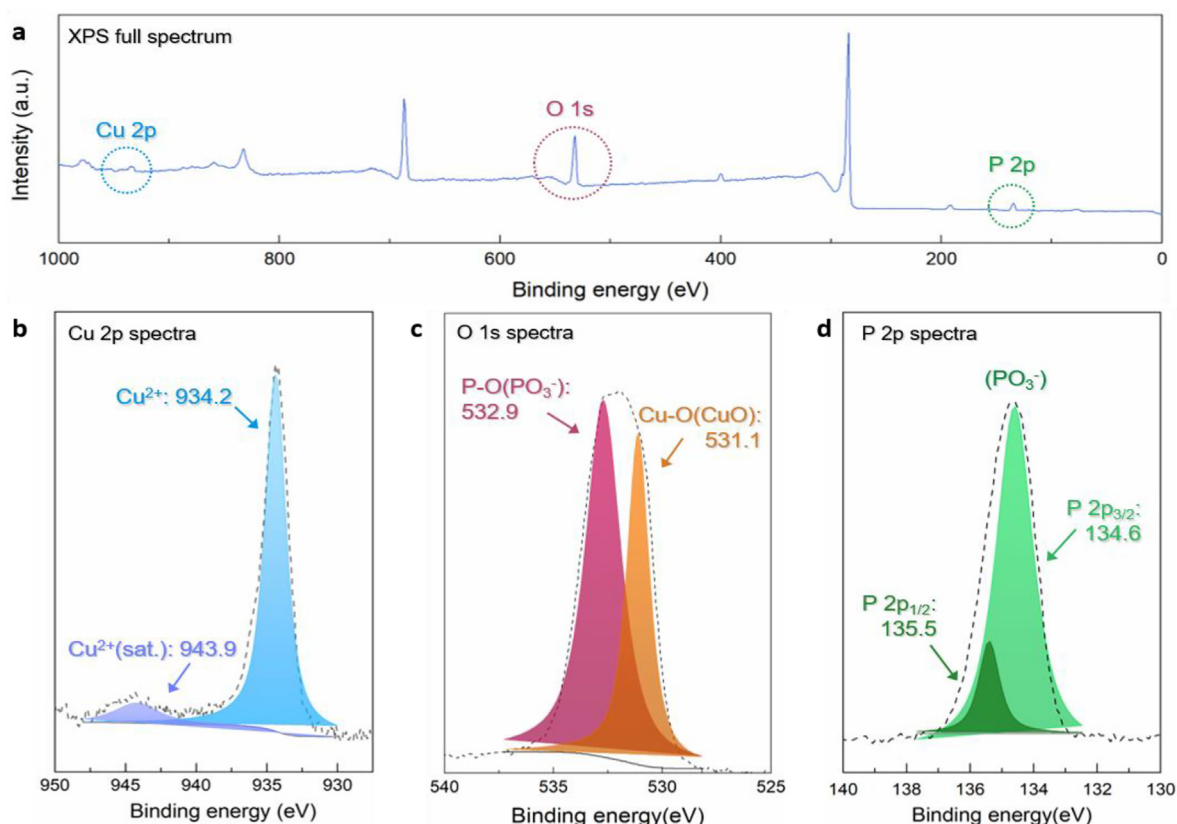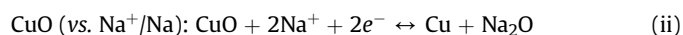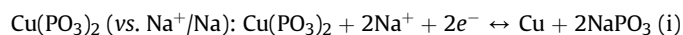

Fig. 3. XPS spectra of *a-c*-CPO: (a) XPS full spectrum, (b) Cu 2p spectra, (c) O 1s spectra, and (d) P 2p spectra.

electron microscopy (SEM) analyses (Fig. 2d–e). Whereas the average particle size of bare Cu(PO$_3$)$_2$ was just the micro-scale, the particle size of *a-c*-CPO decreased to the nano-scale as a result of the ball milling process. SEM-based Energy-dispersive X-ray spectroscopy (EDS) mapping analyses exhibited that both bare Cu(PO$_3$)$_2$ and *a-c*-CPO were composed of homogenously distributed Cu, P, and O elements regardless of amorpholization (Fig. 2f–g). These results were supported by the inductively coupled plasma atomic emission spectroscopy (ICP-OES) results, which identified the atomic ratio of Cu(PO$_3$)$_2$ as Cu:P:O = 1.01:1.99:6.02 (Table S1).

X-ray photoelectron spectroscopy (XPS) analysis was performed to support the material verification of *a-c*-CPO with ambiguous XRD patterns (Fig. 3a). In the Cu 2p XPS spectra (Fig. 3b), Cu was determined to be in the valence state of Cu^{2+} from a strong peak at 934.2 eV and the satellite peak at 943.6 eV, which was consistent with the O 1s XPS spectra that exhibited Cu–O bonds at 531.1 eV (Fig. 3c) [38,39]. Moreover, the O 1s XPS spectra showed another peak at 532.9 eV indicating P–O bonds of (PO$_3^-$), which was also observed as a strong single peak involving P 2p$_{3/2}$ (134.6 eV) and 2p$_{1/2}$ (135.5 eV) orbitals in the P 2p XPS spectra (Fig. 3d) [40]. Based on these XPS spectra results, we concluded that *a-c*-CPO was successfully prepared as intended.

To enhance the redox potential of a material, we aim to maximize the inductive effect using polyanion groups [22,41]. These materials are characterized by the presence of an additional anion with high electronegativity, leading to weakened bonding between O and M ions due to shared O ions, which reduces the gap between bonding and anti-bonding orbitals and increases the material's redox potential. This effect is particularly suitable in Cu(PO$_3$)$_2$, where polyanion groups share their oxygen with anions and TM ions. By maximizing the inductive effect of polyanions, it is possible to increase the average voltage in the Cu(PO$_3$)$_2$ phase and outperform other conversion-type cathode materials, such as simple TM oxides. We compared the theoretical redox potentials of Cu(PO$_3$)$_2$ as a polyanion compound and CuO as a TM oxide compound in the RSB system using first-principle calculation (Table S2). Cu(PO$_3$)$_2$ and CuO undergo the following conversion reactions during the charge/discharge process, respectively:

$$Cu(PO_3)_2 \ (vs. \ Na^+/Na): Cu(PO_3)_2 + 2Na^+ + 2e^- \leftrightarrow Cu + 2NaPO_3 \quad (i)$$

$$CuO \ (vs. \ Na^+/Na): CuO + 2Na^+ + 2e^- \leftrightarrow Cu + Na_2O \quad (ii)$$

The theoretical formation energies for the Cu(PO$_3$)$_2$ and CuO species calculated by first-principles calculation were represented in Table S2. It was verified CuO just expresses an average operation voltage of ~1.2 V (*vs.* Na$^+$/Na). On the other hand, Cu(PO$_3$)$_2$ achieved an average operation voltage of ~3.2 V (*vs.* Na$^+$/Na), which is higher

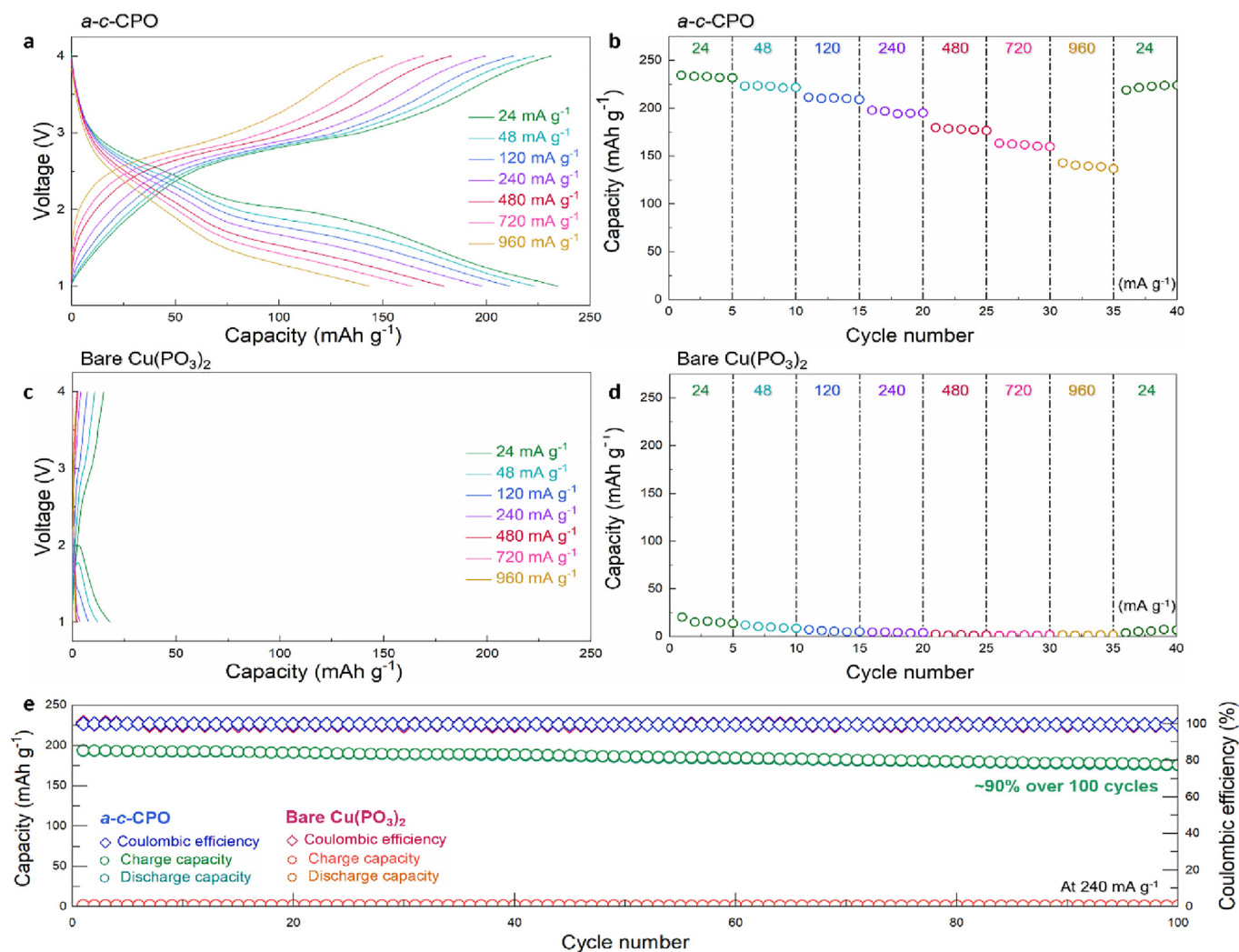**Fig. 4.** Charge/discharge curves and rate capability of (a, b) *a-c*-CPO and (c, d) bare Cu(PO$_3$)$_2$ in the voltage range of 1.0–4.0 V at various discharge current rates. (e) Comparison of cycling performance of *a-c*-CPO and bare Cu(PO$_3$)$_2$ over 100 cycles at 240 mA g^{-1}.

than that of other conversion-type electrode materials for RSBs. Higher theoretical average voltage of $Cu(PO_3)_2$ than that of CuO successfully demonstrates our strategy for achieving a higher redox potential through maximizing inductive effect with poly-anion groups containing high electronegativity elements.

We evaluated the Na storage properties of *a-c*-CPO and bare $Cu(PO_3)_2$ electrodes under the RSB system in the voltage range of 1.0−4.0 V (*vs.* Na^+/Na) after stabilizing with pre-cycle at 24 mA/g. As presented at Fig. S3, there was difference in charge/discharge curves of 1st and 2nd cycles. When the sodium-ions were initially inserted into conversion-type electrode, the structure of material was completely decomposed and rearranged to TM nano-particles and sodium-based composites. Therefore, the structural changes that conversion-type materials undergo during subsequent sodiation/desodiation follow different pathways than those of the initial reactions [42]. Fig. 4a−d showed a comparison of charge/discharge curves and rate performances of *a-c*-CPO and bare $Cu(PO_3)_2$ electrodes at various current densities. It was verified *a-c*-CPO achieved much better electrochemical performances than bare $Cu(PO_3)_2$. The *a-c*-CPO delivered a specific capacity of ~232 mAh/g at 24 mA/g, which corresponds to 2 mol Na^+ storage per formula unit of $Cu(PO_3)_2$. The average operation voltage of *a-c*-CPO under the RSB

system was close to ~2.0 V, higher than other conversion-type cathodes for RSBs [43,44]. Even at high current density of 960 mA/g, *a-c*-CPO still delivered a high specific capacity of ~143 mAh/g with respectable reaction kinetics, corresponding to ~62% of its initial capacity at 24 mA/g. In addition, we conducted cyclic voltammetry test on *a-c*-CPO electrode at 1 mV/s in the voltage range of 1.0−4.0 V and clear cathodic and anodic peaks were observed during cycle (Fig. S4). Furthermore, the cycle performance of *a-c*-CPO was also remarkable. For 100 cycles at 240 mA/g, the specific capacity was retained up to 90% of the initial capacity with high Coulombic efficiency (CE) of above 99% (Fig. 4e). In addition, as presented at Fig. S5, *a-c*-CPO exhibited outstanding electrochemical performance when compared to other cathodes in the RSBs system. Specifically, *a-c*-CPO demonstrated a superior energy density compared to intercalation-type cathodes for RSBs, indicating its high potential as a promising cathode [45−50]. On the other hand, bare $Cu(PO_3)_2$ delivered poor electrochemical properties, such low capacity of ~20 mAh/g at 24 mA/g. Through various measurements, we verified that the *a-c*-CPO electrode stably remained without critical damage despite the significant volume expansion typically experienced by conversion-type cathodes during prolonged cycling (Fig. S6). These observations suggest that
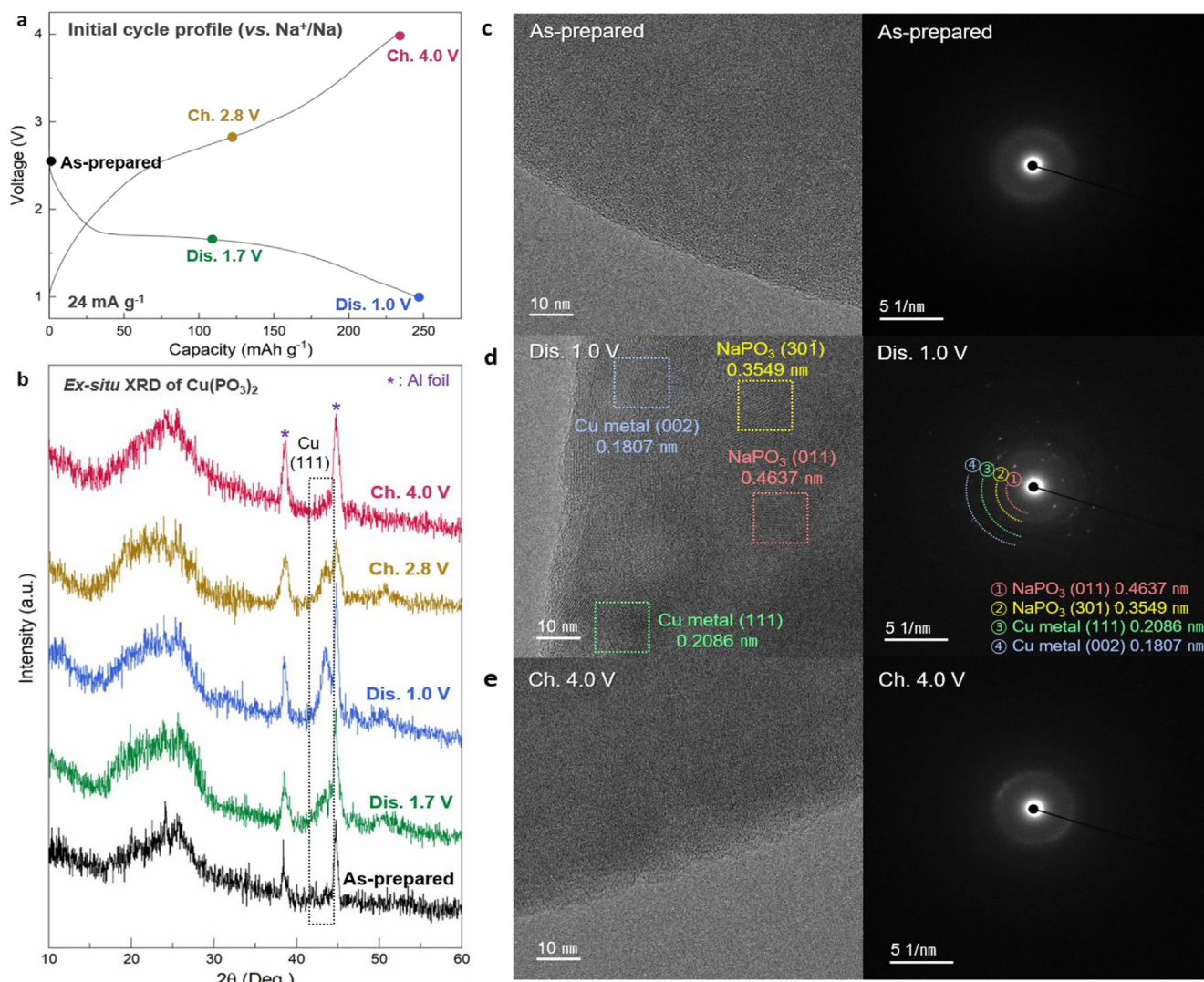

Fig. 5. (a) Initial charge/discharge curves and cut-off voltage points of *ex-situ* samples. (b) *Ex-situ* XRD patterns of *a-c*-CPO electrodes at various voltage. (c−e) HRTEM images and SAED patterns of (c) as-prepared, (d) discharged, and (c) charged *a-c*-CPO composites.

the amorphous phase and the carbon coating in *a-c*-CPO played a critical role in enabling the electrode to withstand severe volume changes. The superior electrochemical performance of *a-c*-CPO than bare $Cu(PO_3)_2$ suggests that the amorphous phase and the carbon-coating of *a-c*-CPO facilitated faster Na^+ diffusion and tolerance for severe volume change under the conversion reaction during charge/discharge process. The electrochemical impedance spectroscopy (EIS) (Fig. S7) was performed to compare the diffusion kinetics of both *a-c*-CPO and bare $Cu(PO_3)_2$. The size of the semi-circle for *a-c*-CPO (144 Ω), which is related to the charge transfer resistance of Na^+, was much smaller than that of bare $Cu(PO_3)_2$ (1005 Ω), implying much faster Na^+ diffusion through the amor-pholization of *a-c*-CPO and supporting the enhanced electro-chemical performances. The *a-c*-CPO electrode also evaluated the electrochemical performances in a full-cell test using a sodiated hard carbon anode (Fig. S8). It was known that the hard carbon anode exhibits the large irreversible capacity at the initial cycle, therefore, we prepared a pre-cycled hard carbon electrode. In addition, the hard carbon was sodiated to provide the Na source to alternate Na metal as an anode electrode during cycling. In the voltage range of 1.9–3.9 V at 240 mA/g, the *a-c*-CPO‖hard carbon cell delivered ~186 mAh/g of initial capacity and maintained 85% capacity retention after 100 cycles at 240 mA/g. The outstanding cyclability results of the *a-c*-CPO‖hard carbon cell indicate that *a-c*-CPO can be considered as a promising conversion-type cathode for RSBs.

Various analyses were used to verify the conversion reaction of $Cu(PO_3)_2$ phase in *a-c*-CPO under the RSB system ($Cu(PO_3)_2$ + $2Na^+$ + $2e^-$ ↔ Cu + $2NaPO_3$). The *a-c*-CPO electrode was charged/discharged to various cut-off voltage with the current

density of 24 mA/g, and various *ex-situ* analyses were performed (Fig. 5a). Firstly, we investigated the structural change during charge/discharge using *ex-situ* XRD analysis (Fig. 5b). Although the XRD patterns of the entire samples were difficult to distinguish due to the amorphous phase, the (111) plane of metallic Cu^0 at 43° (2θ) clearly appeared as sodiation (discharge) progressed to 1.0 V. This implies that the $Cu(PO_3)_2$ phase was decomposed, and the metallic Cu^0 phase was formed through a conversion reaction. The metallic Cu^0 phase disappeared as the desodiation (charge) progressed to 4.0 V, indicating that the metallic Cu^0 was gradually diminished, and the $Cu(PO_3)_2$ phase was restored. Unfortunately, it was difficult to observe the $NaPO_3$ phase at discharge through XRD analysis because the formed/restored phases were low-crystallite or amorphous phases. To clarify the demonstration for the existence of the $NaPO_3$ phase at discharge and conversion reaction of $Cu(PO_3)_2$, HRTEM and SAED analyses were performed (Fig. 5c–e). At the as-prepared electrode, there was one ring pattern corresponding to (022) plane of $Cu(PO_3)_2$ phase. After discharging, the ring patterns corresponding to metallic Cu and $NaPO_3$ phases were detected. And then, it was verified the charged electrode exhibited similar ring pattern with the as-prepared sample. Therefore, these results provide strong evidence for a reversible conversion reaction, supporting the *ex-situ* XRD patterns.

Moreover, we demonstrated the changes in the valence states and local structure of $Cu(PO_3)_2$ phase through synchrotron-based X-ray absorption near edge structure (XANES) and extended X-ray absorption fine structure (EXAFS) analyses (Fig. 6a–b). The Cu K-edge spectra changed to a lower energy state during discharge, indicating the reduction from Cu^{2+} to Cu^0. After charge, the Cu K-edge spectra returned to the Cu^{2+} state, similar to the as-prepared
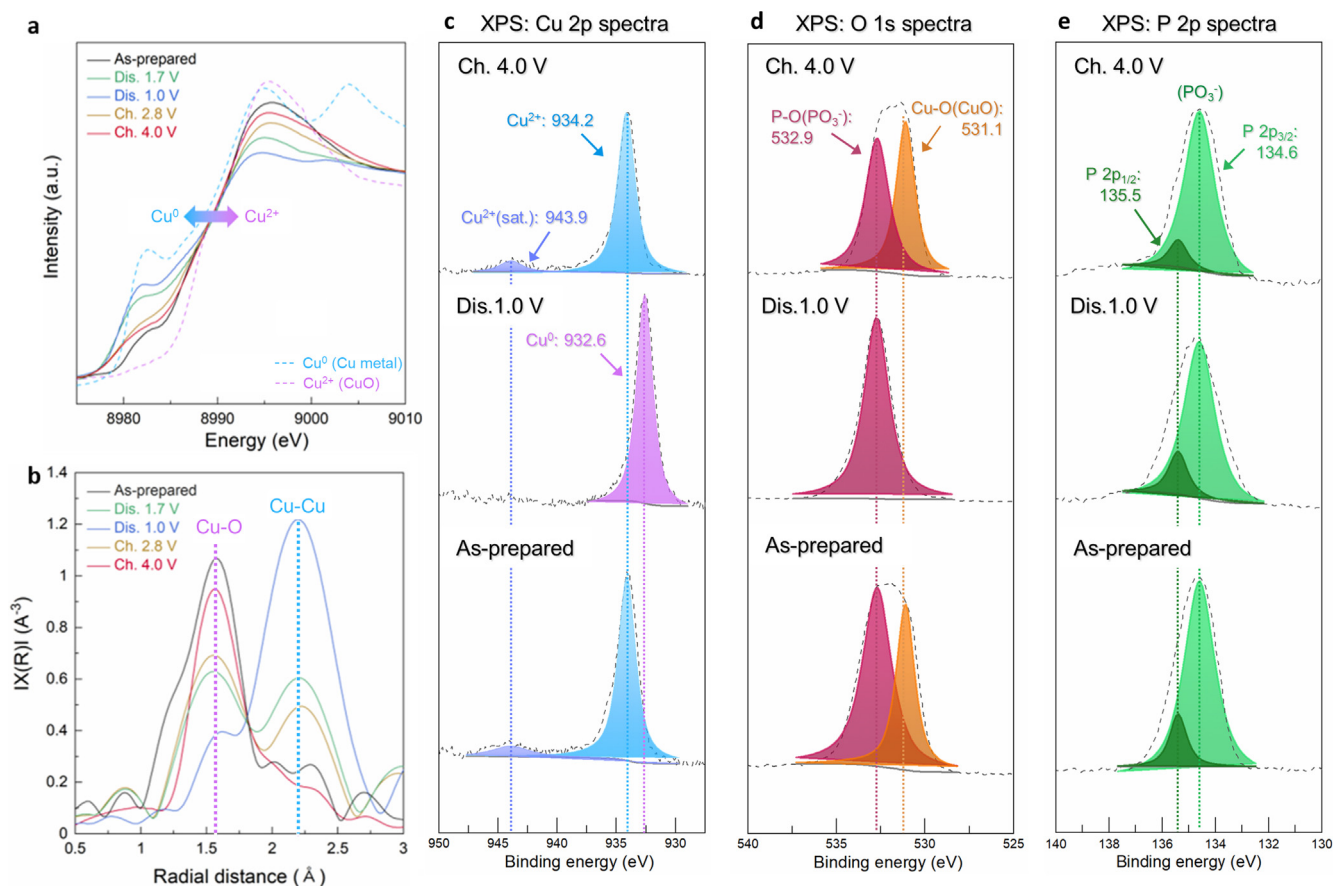

Fig. 6. *Ex-situ* analyses of *a-c*-CPO electrodes on (a) Cu K-edge XANES spectra, (b) Cu K-edge EXAFS spectra, (c) XPS-Cu 2p spectra, (d) XPS-O 1s spectra, and (e) XPS-P 2p spectra during charge/discharge.

electrode. These results indicate the reversible conversion reaction of $Cu(PO_3)_2$ phase in the a-c-CPO under the RSB system. This trend was also observed in ex-$situ$ EXAFS analysis. The Cu−O bond decreased and the Cu−Cu bond increased as discharge progressed, indicating the decomposition of $Cu(PO_3)_2$ and the formation of metallic Cu^0. As charge proceeded, the Cu−O bond was restored and the Cu−Cu bond diminished, indicating the restored $Cu(PO_3)_2$ from decomposed metallic Cu^0. Additionally, the changes in the chemical bonds during the conversion reaction of $Cu(PO_3)_2$ phase in the RSB system were verified through XPS analyses (Fig. 6c−e). After discharge, the peak in the Cu 2p XPS spectra shifted from 934.2 eV (Cu^{2+}) to 932.6 eV (metallic Cu^0), which implies the formation of metallic Cu^0. In the O 1s XPS spectra, the peak at 531.1 eV (Cu−O) disappeared, and only a single peak at 532.9 eV (PO_3^-) corresponding to $NaPO_3$ was maintained. After charge, the peaks returned to the same position as the as-prepared sample in both the Cu 2p and O 1s spectra. In the P 2p XPS spectra, the peak at 134.6 eV (PO_3^-) did not shift and change during charge and discharge, since the (PO_3^-) polyanion always exists in the as-prepared and the charged electrodes (as $Cu(PO_3)_2$) and the discharged electrode ($NaPO_3$). These various ex-$situ$ analyses clearly show occurrence of the reversible conversion reaction of $Cu(PO_3)_2$ phase in a-c-CPO under the RSB system.

4. Conclusion

This study proposes a method for developing an amorphous $Cu(PO_3)_2$ with conductive carbon nanocomposite (a-c-CPO) as a conversion-type cathode for RSBs. The amorpholization and homogeneous carbon-coating by the high energy ball-milling process resulted in successfully enhanced kinetics on the conversion reaction of $Cu(PO_3)_2$ phase in a-c-CPO under the RSB system. At the current density of 24 mA/g, a-c-CPO delivered the large specific capacity of ∼232 mAh/g, whereas bare $Cu(PO_3)_2$ with high crystallinity just showed ∼20 mAh/g at the same conditions. Particularly, its average operation voltage was ∼2.0 V ($vs.$ Na^+/Na), which is much higher than those of general metal-oxide-based conversion electrode materials. The high redox potential of the conversion reaction on $Cu(PO_3)_2$ was attributed to the inductive effect by phosphorus ions with high electronegativity. Furthermore, the capacity of a-c-CPO was retained to ∼90% of its initial capacity after 100 cycles at 240 mA/g, indicating occurrence of reversible and stable conversion reaction during charge/discharge. In addition, through various ex-$situ$ experiments such as XRD, TEM, XANES, EXAFS, and XPS, it was clearly demonstrated the $Cu(PO_3)_2$ phase in a-c-CPO undergoes the following conversion reaction under the RSB system; $Cu(PO_3)_2 + 2Na \leftrightarrow Cu + 2NaPO_3$. This research on a-c-CPO can suggest an effective strategy to overcome the drawbacks of conversion-type cathode and provide significant insight into the study of amorphous cathode.

Credit author statement

Yongseok Lee: Conceptualization, Validation, Investigation, Resources, Writing−Original, Writing−Review & Editing and Visualization. **Jungmin Kang**: Visualization, Formal analysis and Methodology. **Jinho Ahn**: Formal analysis and Validation. **Wonseok Ko**: Investigation, Visualization, Methodology. **Hyunyoung Park**: Validation, Data Curation. **Jung-Keun Yoo:** Investigation, Data Curation. **Won-Sub Yoon**: Project administration, Supervision, Conceptualization, Writing-Review & Editing and Funder. **Jongsoon Kim**: Project administration, Supervision, Visualization, Writing-Review & Editing, Funding acquisition.

Declaration of competing interest

The authors declare that they have no known competing financial interests or personal relationships that could have appeared to influence the work reported in this paper.

Data availability

Data will be made available on request.

Acknowledgement

Appendix A. Supplementary data

Supplementary data to this article can be found online at https://doi.org/10.1016/j.mtener.2023.101325.

References

[1] S.Q. Xiong, J.P. Ji, X.M. Ma, Environmental and economic evaluation of remanufacturing lithium-ion batteries from electric vehicles, Waste Manag. 102 (2020) 579−586, https://doi.org/10.1016/j.wasman.2019.11.013.

[2] C.M. Costa, J.C. Barbosa, R. Goncalves, H. Castro, F.J. Del Campo, S. Lanceros-Mendez, Recycling and environmental issues of lithium-ion batteries: advances, challenges and opportunities, Energy Storage Mater. 37 (2021) 433−465, https://doi.org/10.1016/j.ensm.2021.02.032.

[3] J. Ahn, H.G. Im, Y. Lee, D. Lee, H. Jang, Y. Oh, K. Chung, T. Park, M.K. Um, J.W. Yi, J. Kim, D.J. Kang, J.K. Yoo, A novel organosilicon-type binder for LiCoO_2 cathode in Li-ion batteries, Energy Storage Mater. 49 (2022) 58−66, https://doi.org/10.1016/j.ensm.2022.04.005.

[4] S.A. Han, H. Qutaish, J.W. Lee, M.S. Park, J.H. Kim, Metal-organic framework derived porous structures towards lithium rechargeable batteries, EcoMat 5 (2023), https://doi.org/10.1002/eom2.12283.

[5] B. Dunn, H. Kamath, J.M. Tarascon, Electrical energy storage for the grid: a battery of choices, Science 334 (2011) 928−935, https://doi.org/10.1126/science.1212741.

[6] J.Y. Hwang, S.J. Park, C.S. Yoon, Y.K. Sun, Customizing a Li-metal battery that survives practical operating conditions for electric vehicle applications, Energy Environ. Sci. 12 (2019) 2174−2184, https://doi.org/10.1039/c9ee00716d.

[7] S.K. Lee, W.S. Ko, H. Park, Y.S. Lee, J.M. Kang, J. Ahn, S.Y. Lee, E. Sim, K. Ihm, K.Y. Park, J. Kim, Gradational anionic redox enabling high-energy P2-type Na-layered oxide cathode, Chem. Eng. J. 451 (2023), https://doi.org/10.1016/j.cej.2022.138883.

[8] S. Lee, J. Kang, M.K. Cho, H. Park, W. Ko, Y. Lee, J. Ahn, S. Lee, E. Sim, K. Ihm, J. Hong, H. Kim, J. Kim, High-energy P2-type Na-layered oxide cathode with sequentially occurred anionic redox and suppressed phase transition, Appl. Phys. Rev. 9 (2022), https://doi.org/10.1063/5.0100108.

[9] S.H. Guo, H.J. Yu, Z.L. Jian, P. Liu, Y.B. Zhu, X.W. Guo, M.W. Chen, M. Ishida, H.S. Zhou, A high-capacity, low-cost layered sodium manganese oxide material as cathode for sodium-ion batteries, ChemSusChem 7 (2014) 2115−2119, https://doi.org/10.1002/cssc.201402138.

[10] Y. Gao, H. Zhang, X.H. Liu, Z. Yang, X.X. He, L. Li, Y. Qiao, S.L. Chou, Low-cost polyanion-type sulfate cathode for sodium-ion battery, Adv. Energy Mater. 11 (2021), https://doi.org/10.1002/aenm.202101751.

[11] U. Nisar, R.A. Shakoor, R. Essehli, R. Amin, B. Orayech, Z. Ahmad, P.R. Kumar, R. Kahraman, S. Al-Qaradawi, A. Soliman, Sodium intercalation/de-intercalation mechanism in Na_4MnV(PO_4)_3 cathode materials, Electrochim. Acta 292 (2018) 98−106, https://doi.org/10.1016/j.electacta.2018.09.111.

[12] W. Ko, J.K. Yoo, H. Park, Y. Lee, I. Kang, J. Kang, J.H. Jo, J.U. Choi, J. Hong, S.T. Myung, J. Kim, Exceptionally high-energy tunnel-type $V_{1.5}Cr_{0.5}O_{4.5}H$ nanocomposite as a novel cathode for Na-ion batteries, Nano Energy 77 (2020), https://doi.org/10.1016/j.nanoen.2020.105175.

[13] Y. Lee, C.H. Jo, J.K. Yoo, J.U. Choi, W. Ko, H. Park, J.H. Jo, D.O. Shin, S.T. Myung, J. Kim, New conversion chemistry of CuSO_4 as ultra-high-energy cathode material for rechargeable sodium battery, Energy Storage Mater. 24 (2020) 458−466, https://doi.org/10.1016/j.ensm.2019.07.013.

[14] J. Kim, H. Kim, K. Kang, Conversion-based cathode materials for rechargeable sodium batteries, Adv. Energy Mater. 8 (2018), https://doi.org/10.1002/aenm.201702646.

[15] Y.M. Dai, Q.J. Chen, C.C. Hu, Y.Y. Huang, W.Y. Wu, M.L. Yu, D. Sun, W. Luo, Copper fluoride as a low-cost sodium-ion battery cathode with high capacity,

Chin. Chem. Lett. 33 (2022) 1435−1438, https://doi.org/10.1016/j.cclet.2021.08.050.

[16] S. Sarkar, V. Ahuja, P. Senguttuvan, S.C. Peter, Optimized structural dimensionality of $CuSbS_2$ as an anode aterial in sodium-ion batteries, ACS Appl. Energy Mater. (2023), https://doi.org/10.1021/acsaem.2c03317.

[17] S. Hariharan, K. Saravanan, P. Balaya, alpha-MoO_3: a high performance anode material for sodium-ion batteries, Electrochem. Commun. 31 (2013) 5−9, https://doi.org/10.1016/j.elecom.2013.02.020.

[18] G. Huang, J. Yin, G.D. Zou, Z. Bayhan, W.L. Zhao, F.W. Ming, X.M. Xu, H.F. Liang, O.F. Mohammed, H.N. Alshareef, MXene conversion to V2S3 heterostructure in CS_2 ambient: a novel approach for sodium-ion battery anodes, Mater, Today Energy 30 (2022), https://doi.org/10.1016/j.mtener.2022.101184.

[19] S.R. Dai, L.C. Wang, M.L. Cao, Z.C. Zhong, Y. Shen, M.K. Wang, Design strategies in metal chalcogenides anode materials for high-performance sodium-ion battery, Mater, Today Energy 12 (2019) 114−128, https://doi.org/10.1016/j.mtener.2018.12.011.

[20] X.Y. Tan, R.W. Mo, J.H. Xu, X.R. Li, Q.Y. Yin, L. Shen, Y.F. Lu, High performance sodium ion anodes based on Sn_4P_3 encapsulated within amphiphilic graphene tubes, Adv. Energy Mater. 12 (2022), https://doi.org/10.1002/aenm.202102345.

[21] J.H. Yu, C.H. Jo, H.J. Kim, S.T. Myung, Promising sodium storage of bismuthinite by conversion chemistry, Energy Storage Mater. 38 (2021) 241−248, https://doi.org/10.1016/j.ensm.2021.03.009.

[22] A.K. Padhi, K.S. Nanjundaswamy, J.B. Goodenough, Phospho-olivines as positive-electrode materials for rechargeable lithium batteries, J. Electrochem. Soc. 144 (1997) 1188−1194, https://doi.org/10.1149/1.1837571.

[23] L.M. Lu, G.Q. Jiang, C.Y. Gu, J.F. Ni, Revisiting polyanionic $LiFePO_4$ battery material for electric vehicles, Funct. Mater. Lett. 14 (2021), https://doi.org/10.1142/s1793604721300061.

[24] Y. Lee, J. Kang, J. Ahn, W. Ko, H. Park, S. Lee, S. Lee, J.K. Yoo, J. Kim, A high-energy conversion-type cathode activated by amorpholization for Li rechargeable batteries, J. Mater. Chem. 10 (2022) 20080−20089, https://doi.org/10.1039/d2ta02167f.

[25] J. Yan, J.H. Zhang, J.J. Qi, L. Li, H.W. Luo, Y. Cao, Y. Zhang, Y.L. Ding, L.Z. Wang, Honeycomb-like amorphous VPO_4/C spheres with improved sodium storage performance as anode materials for sodium-ion batteries, Ionics 26 (2020) 3669−3676, https://doi.org/10.1007/s11581-020-03639-w.

[26] L.G. Zhang, L.T. Yu, O.L. Li, S.Y. Choi, G. Saeed, D. Lee, K.H. Kim, Facile synthesis of necessary amorphous structure $FePO_4$ nanospheres as superior sodium-ion battery cathodes, ACS Appl. Energy Mater. 5 (2022) 5954−5963, https://doi.org/10.1021/acsaem.2c00336.

[27] M.S. Wang, A.M. Peng, H. Xu, Z.L. Yang, L. Zhang, J. Zhang, H. Yang, J.C. Chen, Y. Huang, X. Li, Amorphous SnSe quantum dots anchoring on graphene as high performance anodes for battery/capacitor sodium ion storage, J. Power Sources 469 (2020), https://doi.org/10.1016/j.jpowsour.2020.228414.

[28] X. Li, S.H. Guo, K.Z. Jiang, Y. Qiao, M. Ishida, H.S. Zhou, Amorphous P2S5/C composite as high-performance anode materials for sodium-ion batteries, Acs Appl. Mater. Int. 10 (2018) 16−20, https://doi.org/10.1021/acsami.7b14673.

[29] Y.Y. Zhao, Q. Fu, D.S. Wang, Q. Pang, Y. Gao, A. Missiul, R. Nemausat, A. Sarapulova, H. Ehrenberg, Y.J. Wei, G. Chen, Co_9S_8@carbon yolk-shell nanocages as a high performance direct conversion anode material for sodium ion batteries, Energy Storage Mater. 18 (2019) 51−58, https://doi.org/10.1016/j.ensm.2018.09.005.

[30] C.C. Lin, W.H. Lin, S.C. Huang, C.W. Hu, T.Y. Chen, C.T. Hsu, H. Yang, A. Haider, Z.G. Lin, U. Kortz, U. Stimming, H.Y. Chen, Mechanism of sodium ion storage in $Na_7[H_2PV_{14}O_{42}]$ anode for sodium-ion batteries, Adv. Mater. Interfac. 5 (2018), https://doi.org/10.1002/admi.201800491.

[31] S. Niketic, M.C.D. MacNeil, Y. Abu-Lebdeh, Improving the performance of high voltage $LiMn_{1.5}Ni_{0.5}O_4$ cathode material by carbon coating, J. Power Sources 271 (2014) 285−290, https://doi.org/10.1016/j.jpowsour.2014.08.015.

[32] G.X. Wang, L. Yang, S.L. Bewlay, Y. Chen, H.K. Liu, J.H. Ahn, Electrochemical properties of carbon coated $LiFePO_4$ cathode materials, J. Power Sources 146 (2005) 521−524, https://doi.org/10.1016/j.jpowsour.2005.03.201.

[33] G. Kresse, J. Furthmuller, Efficiency of ab-initio total energy calculations for metals and semiconductors using a plane-wave basis set, Comput. Mater. Sci. 6 (1996) 15−50, https://doi.org/10.1016/0927-0256(96)00008-0.

[34] P.E. Blochl, Projector augmented-wave method, Phys. Rev. B 50 (1994) 17953−17979, https://doi.org/10.1103/PhysRevB.50.17953.

[35] J.P. Perdew, K. Burke, M. Ernzerhof, Generalized gradient approximation made simple, Phys. Rev. Lett. 77 (1996) 3865−3868, https://doi.org/10.1103/PhysRevLett.77.3865.

[36] V.I. Anisimov, F. Aryasetiawan, A.I. Lichtenstein, First-principles calculations of the electronic structure and spectra of strongly correlated systems: the LDA+U method, J. Phys. Condens. Matter 9 (1997) 767−808, https://doi.org/10.1088/0953-8984/9/4/002.

[37] A. Jain, S.P. Ong, G. Hautier, W. Chen, W.D. Richards, S. Dacek, S. Cholia, D. Gunter, D. Skinner, G. Ceder, K.A. Persson, Commentary: the Materials Project: a materials genome approach to accelerating materials innovation, Apl. Mater. 1 (2013), https://doi.org/10.1063/1.4812323.

[38] L.N. Xu, J. Li, H.B. Sun, X. Guo, J.K. Xu, H. Zhang, X.J. Zhang, In situ growth of Cu2O/CuO nanosheets on Cu coating carbon cloths as a binder-free electrode for asymmetric supercapacitors, Front. Chem. 7 (2019), https://doi.org/10.3389/fchem.2019.00420.

[39] Y.J. Gao, F.Y. Yang, Q.H. Yu, R. Fan, M. Yang, S.Q. Rao, Q.C. Lan, Z.J. Yang, Z.Q. Yang, Three-dimensional porous Cu@Cu_2O aerogels for direct voltammetric sensing of glucose, Microchim. Acta 186 (2019), https://doi.org/10.1007/s00604-019-3263-6.

[40] NIST X-ray Photoelectron Spectroscopy Database. https://doi.org/10.18434/T4T88K (accessed 24 April 2023).

[41] C.F. Liu, Z.G. Neale, G.Z. Cao, Understanding electrochemical potentials of cathode materials in rechargeable batteries, Mater. Today 19 (2016) 109−123, https://doi.org/10.1016/j.mattod.2015.10.009.

[42] J. Li, S. Hwang, F. Guo, S. Li, Z. Chen, R. Kou, K. Sun, C.J. Sun, H. Gan, A. Yu, E.A. Stach, H. Zhou, D. Su, Phase evolution of conversion-type electrode for lithium ion batteries, Nat. Commun. 10 (2019) 2224, https://doi.org/10.1038/s41467-019-09931-2.

[43] M.K. Aslam, T. Hussain, H. Tabassum, Z. Wei, W. Tang, S. Li, S.-j. Bao, X.S. Zhao, M. Xu, Sulfur encapsulation into yolk-shell Fe_2N@nitrogen doped carbon for ambient-temperature sodium-sulfur battery cathode, Chem. Eng. J. 429 (2022), https://doi.org/10.1016/j.cej.2021.132389.

[44] Y.-N. Zhou, M. Sina, N. Pereira, X. Yu, G.G. Amatucci, X.-Q. Yang, F. Cosandey, K.-W. Nam, $FeO_{0.7}F_{1.3}$/C nanocomposite as a high-capacity cathode material for sodium-ion batteries, Adv. Funct. Mater. 25 (2015) 696−703, https://doi.org/10.1002/adfm.201403241.

[45] K. Mathiyalagan, A. Ponnaiah, K. Karuppiah, S. Rengapillai, S. Marimuthu, Enhanced performance on layered O3-$Na_{0.95}CrO_2$ cathode material for emerging sodium-ion batteries, Ionics 26 (2020) 3929−3936, https://doi.org/10.1007/s11581-020-03523-7.

[46] X. Luo, Q. Huang, Y. Feng, L. Zhou, W. Wei, Designing layered $Na_3Ni_2SbO_6$ cathodes with hierarchical and hollow nanostructure for sodium-ion batteries, Chemelectrochem 9 (2022), https://doi.org/10.1002/celc.202200821.

[47] G. Tang, Z. Chen, Z. Lin, S. Luo, T. Chen, J. Chen, W. Xiang, W. Li, M. Chen, K+-doped P2-$Na_{0.67}Fe_{0.5}Mn_{0.5}O_2$ cathode for highly enhanced rate performance sodium-ion battery, J. Alloys Compd. 947 (2023), https://doi.org/10.1016/j.jallcom.2023.169482.

[48] J. Zhao, X. Zhang, J. Wang, X. Yang, J. Deng, Y. Wang, P2-type $Na_{0.59}Co_{0.20}Mn_{0.77}Mo_{0.03}O_2$ cathode with excellent cycle stability for sodium-ion batteries, J. Solid State Electrochem. 24 (2020) 1349−1361, https://doi.org/10.1007/s10008-020-04547-9.

[49] B. Peng, Y. Chen, L. Zhao, S. Zeng, G. Wan, F. Wang, X. Zhang, W. Wang, G. Zhang, Regulating the local chemical environment in layered O3-$NaNi_{0.5}Mn_{0.5}O_2$ achieves practicable cathode for sodium-ion batteries, Energy Storage Mater. 56 (2023) 631−641, https://doi.org/10.1016/j.ensm.2023.02.001.

[50] X. Chen, Z. Zhao, K. Huang, H. Tang, Al-substituted stable-layered P2-$Na_{0.6}Li_{0.15}Al_{0.15}Mn_{0.7}O_2$ cathode for sodium ion batteries, Int. J. Energy Res. 45 (2021) 11338−11345, https://doi.org/10.1002/er.6606.